Analyst

PAPER

View Article Online
View Journal

Cite this: DOI: 10.1039/d5an01007a

Predictive analysis of organic semiconductor photodegradation by FTIR spectroscopy with multivariate analysis

Sarah M. Tyler, Thomas J. Blackburn, Kellen T. Schneider and Jeanne E. Pemberton *

Received 20th September 2025,
Accepted 24th March 2026

DOI: 10.1039/d5an01007a

rsc.li/analyst

Organic semiconductors (OSCs) serve as the essential elements of emerging next-generation optoelectronic devices. These devices continue to experience advances in overall efficiency, but their long-term implementation is challenged by complex and often poorly understood degradation processes that can involve not only the OSC active component but also contacts and charge carrier transport layers. Better tools are needed to characterize chemical and photochemical degradation of these components *in operando*. Here, attenuated total reflectance-FTIR (ATR-FTIR) spectroscopy combined with multivariate analysis is demonstrated as a diagnostic tool for monitoring degradation of thin films of poly[[4,8-bis[(2-ethylhexyl)oxy]benzo[1,2-*b*:4,5-*b*']dithiophene-2,6-diyl][3-fluoro-2-[(2-ethylhexyl)carbonyl]thieno[3,4-*b*]thiophenediyl]] (PTB7), an active layer material used in organic photovoltaics, as a model high-performance OSC. Multivariate analysis of the resulting FTIR spectral data is shown to be effective at identifying pristine (not degraded) *versus* degraded samples with high accuracy in accelerated photodegradation experiments. These results highlight the potential of practical diagnostic applications of multivariate analysis to assessment of OSC degradation.

Introduction

Organic photovoltaic devices (OPVs) based on organic semiconductors (OSCs) are recognized as a promising avenue for future solar energy production. Their light weight, flexibility, transparency, and solution processability make them an attractive option for novel applications ranging from solar windows to agrivoltaics.[1–3] Recently, development of non-fullerene acceptors, coupled with advances in device fabrication and design, have resulted in OPV power conversion efficiencies (PCEs) of almost 20%.[4–7] This progress suggests that OPVs with PCEs >20% are imminent,[8,9] thereby enhancing the commercial viability of OPVs as an emerging source of solar-based power.

However, even as higher efficiency materials continue to be designed and tested, the field must contend with its biggest obstacle: chemical stability of active layer materials and their interfaces with other materials. It is well recognized that OPVs are susceptible to a range of degradative environmental conditions including incursion by oxygen and water vapor that, when coupled with radiant exposure, can lead to chemical reactions of active layer materials as well as catalyze interfacial reactions between device layers.[10,11] Along with improved encapsulation methods and more robust chemical systems, practical implementation of OPVs will require inexpensive and accessible analytical methods to monitor the long-term degradation of working devices in the field.

Monitoring chemical degradation in a working OPV device involves overcoming challenges not present in a laboratory setting. Besides the degradation of the organic active layer, the photovoltaic (PV) module portion of a device is also susceptible to environmental conditions. For example, the performance of an OPV can decrease from accumulation of dust or biological soiling, corrosion of PV module packaging, or delamination at various device interfaces.[12] Therefore, simple power output measurements are not sufficient for determining the root cause for decreases in device PCE. Instead, techniques that specifically probe chemical changes of the active layer material itself *via* spectroscopy, preferably non-destructively, are needed to determine if device failure stems from chemical degradation. Here, we propose the use of FTIR spectroscopy coupled with multivariate analysis to diagnose the degradation extent, or relative "age", of a given OPV material. As the use of OPVs and other PV technology has increased in recent years, more attention has been paid to the recyclability of the major device components so that some portions of PV modules can be reused or replaced easily.[13,14] A multivariate analysis-based spectroscopic tool that inexpensively and quickly diagnoses if chemical degradation is causing low device PCE would

Department of Chemistry and Biochemistry, University of Arizona, 1306 East University Boulevard, Tucson, AZ 85721, USA. E-mail: pembertn@arizona.edu

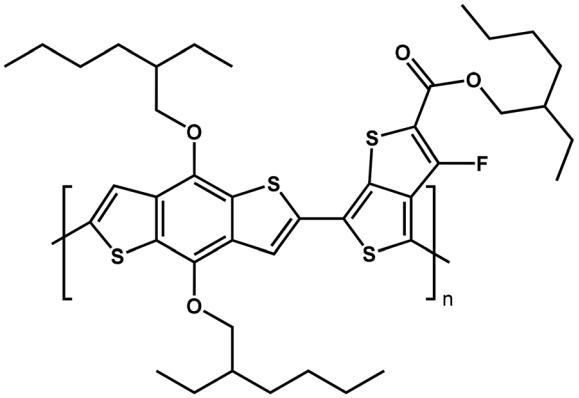

Fig. 1 Molecular structure of poly[[4,8-bis[(2-ethylhexyl)oxy]benzo[1,2-*b*:4,5-*b*′]dithiophene-2,6-diyl][3-fluoro-2-[(2-ethylhexyl)carbonyl]thieno[3,4-*b*]thiophenediyl]] (PTB7), a common organic semiconducting polymer for OPVs.

empower users to make cost-efficient decisions about device repair or replacement.

In this work, we use poly[[4,8-bis[(2-ethylhexyl)oxy]benzo[1,2-*b*:4,5-*b*′]dithiophene-2,6-diyl][3-fluoro-2-[(2-ethylhexyl)carbonyl]thieno[3,4-*b*]thiophenediyl]] (PTB7, Fig. 1) as a model high-performance OSC active layer exposed to solar radiation to demonstrate the utility of attenuated total reflectance-FTIR (ATR-FTIR) coupled with multivariate analysis for true predictive assessment of the degradative chemical state of an OSC. Along with repeated stratified *k*-fold cross validation analysis, the model is tested using spectral data acquired and processed by independent researchers from true unknown PTB7 films to model field-relevant scenarios. Overall, these results provide strong evidence for the utility of such approaches in chemical diagnostics of OPV systems.

Experimental methods

Film preparation

Prior to deposition of PTB7 films, trapezoidal ZnSe internal reflection elements (IREs), 50 mm (long edge) × 10 mm × 2 mm with edges beveled at 45° to allow 13 sampling points by the IR beam, were obtained from New Era Enterprises or Crystran LTD. These IREs were sequentially cleaned with a series of three solvents, hexanes, acetone and isopropanol, by sonicating in each for 5 min. After sonication, the IREs were dried in a stream of N_2 gas prior to film deposition.

Films of PTB7 (Ossila, MW 234 779 g mol^{-1}, PDI 2.82) were spin cast onto IREs held in an in-house built chuck on a Laurell WS-650MZ-23NPP/Lite spin coater that kept the IRE surface level with the surface of the surrounding chuck for uniform spin off of the deposited solution. Films on IREs were deposited from a 10 mg mL^{-1} chlorobenzene solution that was prepared by sonication for 60–90 min at ambient temperature to achieve complete PTB7 dissolution. Films were cast onto ZnSe IREs spinning at 2000 rpm by depositing a 400 μL aliquot of PTB7 solution within the first 5 s of spinning; spinning was continued for a total of 40 s. After spin casting, films were annealed on a hotplate at 80 °C for 1 min. For this deposition protocol, a film thickness of ~20 nm was determined using atomic force microscopy (AFM) on a Park Systems NX20 AFM.

Radiant exposure and ATR-FTIR spectroscopy

Samples were exposed in ambient to AM 1.5G radiation from a Newport Oriel LCS-100 Small Area Sol1A solar simulator that was outfitted with a 100 W ozone-free Xe lamp passed through an AM 1.5G spectral correction filter. Samples were placed at a distance of 7-in beneath the output flange of the simulator to attain a Class A spectral match to the solar irradiance spectrum. Samples were subjected to accelerated degradation conditions by direct exposure to the solar radiation for 30 min intervals for a total of 10 intervals taken for a cumulative 5 h of radiant exposure.

ATR-FTIR measurements were made on a ThermoFisher Scientific Nicolet 6700 FTIR using a custom ATR cell designed and built in-house. The spectral background and sample spectra were acquired for 512 scans at 4 cm^{-1} resolution with a gain of 8. For the training spectral dataset, four independent PTB7 films were prepared, and spectra were acquired for each independent film at three unique ATR trajectories through the film/IRE combination after each radiant exposure interval to create a database of spectral data with 12 samples per radiant exposure interval for a total sample size of 132 spectra. For the independent test spectral dataset, two PTB7 samples were prepared with spectra taken in triplicate at each radiant exposure interval for a total sample size of 66 spectra per trial.

Data analysis

Baseline correction of raw spectral data was performed in OriginPro (OriginLab Corporation, Northampton, MA) over the range of 1000–3400 cm^{-1} using asymmetric least squares smoothing. An asymmetric factor of 10^{-4}, threshold value of 0.005, smoothing parameter between 2.5–4.0, and 25 iterations were used to calculate the baseline subtracted from each spectrum. After baseline correction, spectra were normalized to the 2960 cm^{-1} $\nu(CH_2)$ band, a band that does not change significantly in intensity upon irradiation, to correct for any effects of minor film thickness differences between samples.

Generalized two-dimensional correlation spectroscopy (2D-COS) was performed using the 2D Correlation Spectroscopy Analysis application in OriginPro. The spectral data used for the dynamic spectral dataset was obtained by averaging across the processed ATR-FTIR spectra acquired after each exposure interval. The average of this dynamic spectral dataset was then used as the reference spectrum. Principal component analysis (PCA) was performed in OriginPro. Linear discriminant analysis (LDA) and combined PCA-LDA were performed with an in-house Python script adapted from code obtained from Nirpy Research.[15] This script was modified to evaluate the accuracy of both LDA and PCA-LDA and predict the group classification (total radiant exposure) of unknown samples; the modified script is available on GitHub.[16]

Results and discussion

ATR-FTIR spectroscopy was used to create training spectral datasets of pristine and degraded PTB7 samples formed under accelerated degradation conditions by direct film exposure to radiation from a solar simulator in ambient conditions for different times. Fig. 2 shows a series of normalized and averaged ATR-FTIR spectra between 1000–2000 and 2700–3400 cm^{-1} from PTB7 for pristine films and films exposed to AM 1.5G radiation in a series of 10 sequential 30 min intervals. Full spectra between 1000 and 3400 cm^{-1} for the same conditions are shown in Fig. S1 of the SI. As these spectra document, spectral changes are observed that are a systematic function of radiant exposure time indicating PTB7 photodegradation at multiple functional group sites.

It is noted that minimal changes in spectral intensity are observed for bands in the ν(C–H) region, suggesting that the alkyl chain portions of PTB7 are relatively immune to significant degradation. Thus, these vibrational bands are useful for normalization of the spectral intensities to correct for small sample-to-sample differences in film thickness.

The dark blue trace in Fig. 2 represents the averaged spectrum from pristine PTB7 films. To supplement vibrational assignments previously reported in the literature,[17–22] semi-empirical quantum mechanical predictions were performed individually on the benzodithiophene (BDT) and 3-fluoror-thienothiophene (FTT) subunits. Tabulated values of characteristic vibrational band assignments, along with further description of the semi-quantum method employed for prediction of vibrational frequencies, are provided in Table S1 of the SI and have been discussed in detail previously from this laboratory.[23] Characteristic PTB7 bands are observed at 1059 (ν_s(C–O–C)$_{ether}$ + δ(C–C–C)$_{Th}$), 1153 (ν(C–C)$_{alkyl}$ + ν_s(C–O–C)$_{ester}$), 1261 (ν_{as}(C–O–C)$_{ether}$ + ν_{as}(C–O–C)$_{ester}$ + ν(C–C–C)$_{TP}$), 1294 (ν_{as}(C–O–C)$_{ester}$ + δ(CH$_2$)$_{alkyl}$), 1363 (ν(C=C)$_{TP}$), 1400 and 1431 (ν(C=C)$_{\phi\ ring}$ + ν(C=C)$_{TP}$), 1460 (δ_{as}(CH$_2$)$_{alkyl}$), 1568 (ν_s(C–C–F)$_T$ + ν(C=C)$_{\phi\ ring}$ + ν(C=C)$_{TP}$ + ν(C=C)$_T$), 1705 (ν(C=O)$_{ester}$), 1724 (ν(C=O)$_{ester}$ + ν_{as}(C–C–F)$_T$), 2860 (ν(CH$_2$)$_{alkyl}$), 2871 (ν(CH$_3$)$_{alkyl}$), 2929 (ν(CH$_2$)$_{alkyl}$), and 2960 (ν(CH$_3$)$_{alkyl}$) cm^{-1}.

Upon exposure to solar radiation, multiple spectral regions exhibit either an increase or decrease in intensity. Notably, a slight decrease in intensity of the ν(C=C) band at 1400 cm^{-1} is observed suggesting oxidation of the conjugated backbone. This has been previously attributed to photooxidation of one of the thiophene rings associated with the BDT subunit.[23–26] Additionally, the appearance of a weak band at ~1660 cm^{-1} is assigned to a thioester species attributed to [2 + 2] O_2 cycloaddition with subsequent thioester formation on the BDT subunit.[23,24] Recent X-ray photoelectron spectroscopy (XPS) studies from this laboratory substantiate the presence of such oxidized sulfur species.[23] Collectively, these spectral changes point to photooxidation of the PTB7 films as detailed in recent studies from this laboratory[23] and others.[24–26] Indeed, prior studies have shown this PTB7 degradation process to be driven primarily by the formation and reaction of singlet oxygen ($^1O_2$) *via* energy transfer from long-lived PTB7 polymer triplet states.[27]

To aid in the determination of spectral regions in which the most significant changes occur upon photodegradation, 2D-COS is performed on this series of ATR-FTIR spectra. Although quite common in the NMR field, the time scales of phenomena probed by optical spectroscopies have hindered the development of analogous 2D correlation techniques for vibrational spectroscopic methods such as ATR-FTIR spectroscopy.[28] In general, correlation analysis provides insight into the similarity or dissimilarity of two functions that vary with respect to an external variable,[29] such as radiant exposure time in this work. Developed by Noda in the early 1990s, generalized 2D-COS compares spectral intensity changes at two given spectral variables over the fixed interval of an external variable such as time. After collection of a spectral data set, dynamic spectra are generated by calculating the difference between each collected spectrum and a defined reference spectrum (normally the average spectrum of the dataset[30]). Generalized 2D correlation is then carried out, with the dynamic spectrum treated as a complex number function with real and imaginary components. In this process, every spectral variable in the collected dataset is systematically correlated against every other spectral variable over that fixed interval to generate two, two-dimensional contour plots: the synchronous and asynchronous 2D-COS contour plots. These 2D correlation plots are generated either *via* fast Fourier transformation or Hilbert-Noda transformation of the dynamic spectrum, from which information about the simultaneous and sequential changes occurring at different frequencies can be obtained.[28,29,31] The generic nature of the technique allows it

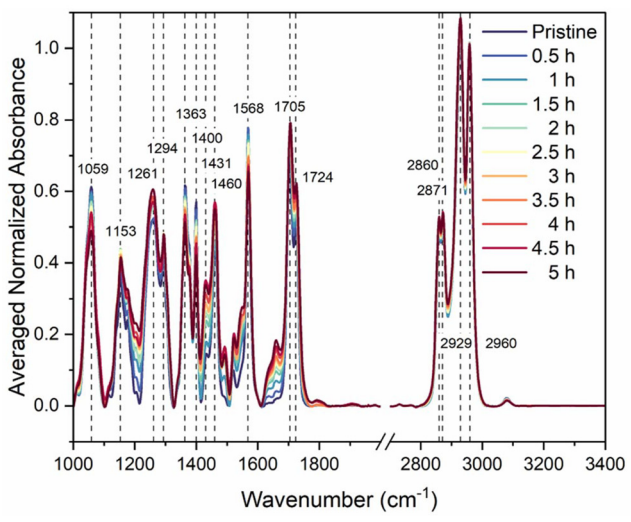

Fig. 2 A series of ATR-FTIR spectra from ~20 nm-thick PTB7 thin films spin cast onto ZnSe IREs with cumulative 30 min exposures in ambient to radiation from a solar simulator. Spectra were acquired in three different regions of each of 4 independently prepared films sample using 512 scans at 4 cm^{-1} resolution. After baseline correction, the resulting 12 spectra for each exposure condition were normalized in intensity to the 2960 cm^{-1} $\nu(CH_2)$ band to correct for effects of minor differences in film thickness between samples and then averaged.

to be applied to any spectral dataset that is obtained from monitoring a system exposed to an external perturbation regardless of the collection technique or instrumental set up.[32] For the uninitiated reader, the mathematical steps of the correlation analysis are elaborated in greater detail in section III of the SI, along with a simple concrete example as demonstrated in Fig. S2–S4. For a more in-depth discussion, the reader is directed to works published by Noda and others that more extensively cover the topic.[28,29,32,33]

The synchronous 2D-COS contour plot is presented in Fig. 3a; this plot gives insight into any correlated intensity changes that stem from exposure to the external perturbation. The peaks located on the diagonal line with coordinates $\nu_1 = \nu_2$ in this synchronous plot are called "autopeaks" and represent frequency regions with significant spectral intensity variation across the dataset, *i.e.*, frequency regions that, in this work, report on photodegradation. The coordinates of peaks located off the diagonal, or "cross peaks", correspond to frequency regions where spectral intensity changes occur simultaneously, with positive peaks (orange/red) indicating intensity changes in the same direction (both increasing or both decreasing in intensity) and negative peaks (green/blue) indicating intensity changes in opposite directions.

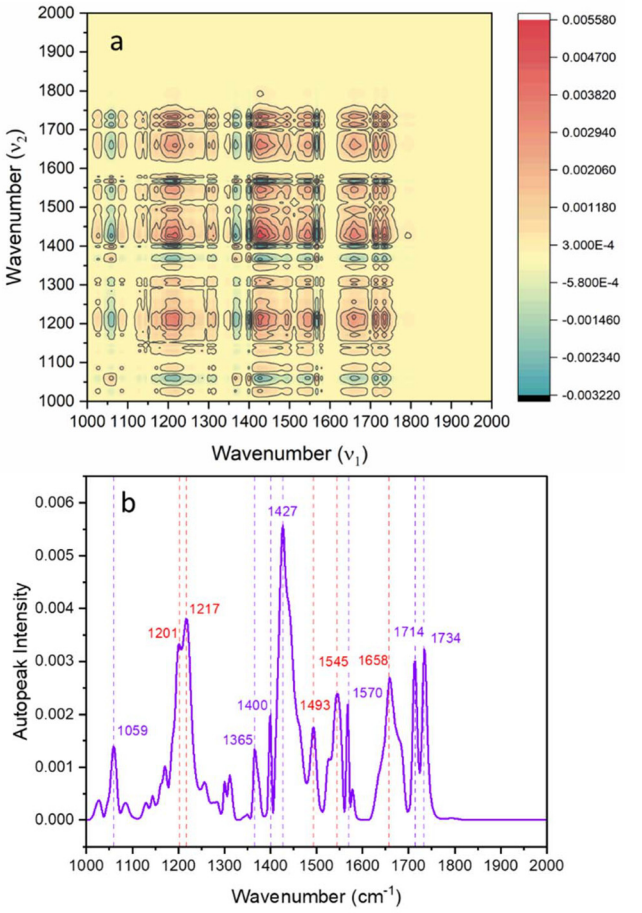

Fig. 3 (a) Synchronous 2D-COS plot from centered ATR-FTIR spectral data for PTB7 films degraded with cumulative 30 min radiant exposures. Spectra were normalized and averaged. The average from the spectral dataset was used as the reference spectrum for 2D-COS calculation. Yellow regions represent frequency coordinate pairs where no correlated spectral intensity changes occur. (b) Power spectrum taken along the $\nu_1 = \nu_2$ diagonal of the 2D-COS synchronous plot visualized as a one-dimensional line cut that more clearly shows the relative intensities of the autopeaks. Power spectrum peaks identified with purple dashed lines and labels correspond to bands present in the pristine spectrum while power spectrum peaks marked with red dashed lines and labels correspond to new spectral bands in heavily overlapped frequency regions.

The power spectrum of the synchronous plot taken along the $\nu_1 = \nu_2$ diagonal is shown in Fig. 3b. Although the power spectrum may resemble the one-dimensional trace of the original dataset, it differs from the original dataset in that the static (unchanging) components of the spectra have been removed through the process of 2D-COS. Although not commonly used by many researchers,[34] the power spectrum offers an accessible way of comparing autopeak intensities in a 2D-COS plot that is easier to interpret, since the only peaks present are those for which spectral intensity changes occur, and the intensities of these peaks are directly proportional to the extent of spectral change during the radiant exposure.

In the synchronous 2D-COS plot of the training dataset, several autopeaks are observed that correspond to frequencies of significant intensity changes. Autopeaks in the synchronous 2D-COS plot corresponding to bands present in the pristine spectrum are observed at 1059, 1365, 1400, 1427, 1570, 1714 and 1734 cm^{-1} (see power spectrum in Fig. 3b) along with peaks at 1201, 1217, 1493, 1545, and 1658 cm^{-1} that suggest the emergence of new spectral bands at heavily overlapped frequencies. For example, the two autopeaks at 1201 and 1217 cm^{-1} fall into a congested spectral region containing ether (ν_{as}(C–O–C)) and ester (ν(C–O)) bands[18] while the autopeak at 1658 cm^{-1} suggests the emergence of a thioester degradation product.[19,23]

For 5 h of radiant exposure, the most intense autopeak in the synchronous 2D-COS plot occurs at 1427 cm^{-1} with a corresponding negative cross peak at (1427, 1570 cm^{-1}). Given that the intensity of the spectral region around 1427 cm^{-1} visually increases with photodegradation, it can be concluded that the 1570 cm^{-1} peak decreases concomitantly. The 1570 cm^{-1} band has previously been assigned to a ν(C=C)[18,21] mode, and the band at 1427 cm^{-1} is in the middle of a frequency region within which aromatic ring stretches are known to occur.[35,36] These spectral changes are consistent with the picture delineated above in which oxidative chemical changes along the main backbone of the polymer occur through photooxidation. Although these processes may lead to multiple degradation products, the 2D-COS analysis is consistent with predominant formation of a thioester product through [2 + 2] O_2 cycloaddition of singlet oxygen that breaks the conjugation, and hence, the ability of the film to transport charge carriers, thereby affecting device PCE. A simplified schematic of this proposed process is shown in Fig. 4. Despite this complexity and the attendant uncertainty about exact chemical species formed, the spectral changes are robust and reproducible,

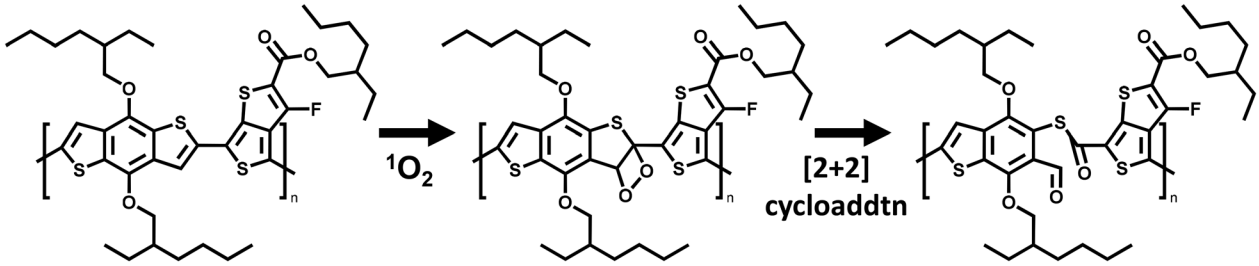

Fig. 4 Schematic of the photooxidation process of PTB7 by [2 + 2] cycloaddition of $^1O_2$ that results in a thioester product responsible for the degradation product peak at ~1660 cm^{-1} in the FTIR spectra and destroys π conjugation along the polymer backbone by breaking a thiophene double bond.

which renders them amenable to development of a reliable diagnostic tool for degradation.

Overall, the increase in oxidized species present in the polymer and spectral changes at frequencies attributed to vibrational modes of the aromatic backbone indicate significant degradation in the PTB7 film which, in a working device, would likely reduce the PCE. To the untrained eye, some of these spectral changes are easy to miss, especially in the early degradation stages. Therefore, the development of a tool that can mathematically discriminate pristine from degraded OPV films would be extremely useful for the average OPV user when attempting to determine principal cause of low PCE.

One goal of this work was to determine the potential for use of ATR-FTIR spectroscopy as a predictive diagnostic tool for analyzing the progression of OSC chemical degradation. Toward that end, two multivariate techniques, PCA and LDA, were employed. These two methods are used to reduce the large number of variables present in spectral datasets. In spectral data such as the photodegradation ATR-FTIR dataset collected in this work, each spectral unit (here, *e.g.*, each cm^{-1}) is a distinct variable with its attendant absorbance value. Thus, any single spectrum contains a large number of variables, many of which are redundant in terms of containing useful information. Since a large number of variables is hard to quantitatively manage, these variable reduction tools are useful in refining the dataset such that only those variables that contain useful information (*i.e.* distinguishing spectral features) are retained. After preprocessing a dataset (which can include steps such as baseline correction and/or normalization), the data are formatted into a matrix from which fewer "new" variables are calculated from linear combinations of the original variables in the dataset. These new variables, called principal components (PCs) or linear discriminants (LDs) for PCA or LDA, respectively, contain the distinguishing spectral information among component spectra in the dataset. More in-depth discussion on PCA and LDA can be found in selected tutorials.[15,37–40] The main difference between PCA and LDA is that PCA is an unsupervised method and as such, is not a classification tool, but instead reduces data dimensionality and calculates new variables (principal components) that maximize the variance between spectra. Each principal component accounts for a percentage of variance in the spectral data, and for visualization purposes, it is common practice to plot the two PC scores that represent the largest variance. LDA, as a supervised multivariate method, relies on user input group or classification labels to calculate new variables (linear discriminants) that maximize group-to-group variation of a training spectral dataset. Similarly, it is common practice to plot the two LD scores that represent the largest variance. These linear discriminants can then be used to predict the classification of unknown samples.[41] Oftentimes, the two are combined by first calculating the principal components for a training dataset and then using these principal components to subsequently calculate linear discriminants for predictive purposes.

For this study, PCA-LDA was performed over two frequency regions of the PTB7 spectral training dataset to explore differences in predictive accuracy. The first region between 1300 and 1900 cm^{-1} contains several spectral envelopes of major intensity change; this region contains very little frequency space without spectral activity as can be observed in the 2D-COS synchronous plot (Fig. 3a) and power spectrum (Fig. 3b). The second region represents the spectral range of 1000 to 3400 cm^{-1} which includes large spectrally-silent frequency regions. The expectation that underpins this comparison was that the narrower but more spectrally active frequency region would yield more accurate training results, because the spectrum-to-spectrum differences between groups would be better represented in the calculated principal components and linear discriminants.

Prior to PCA-LDA, both PCA and LDA were applied independently to the spectral data for later comparison to the more robust PCA-LDA approach. For the unsupervised technique of PCA, the first two principal components account for 79% and 72% of the variance for the 1300–1900 cm^{-1} region and the 1000–3400 cm^{-1} region, respectively. However, for the superior supervised method of LDA, the first two linear discriminants total >95% of the spectral variance for both frequency regions (see Table 1). These LDA results are shown in Fig. 5a and b for the 1300–1900 cm^{-1} and the 1000–3400 cm^{-1} regions, respectively. Using stratified *k*-fold cross validation with 10 splits and 3 repeats, a mean accuracy score of 99.7% is calculated for the 1300–1900 cm^{-1} region, while that for the 1000–3400 cm^{-1} region is 82.3%. However, for both cases, the number of spectral variables (600 and 2400 cm^{-1}, respectively) greatly outnumbers the sample size of the dataset, which can lead to overfit-

Table 1 Calculated linear discriminants for PTB7 ATR-FTIR spectral data between 1300–1900 and 1000–3400 cm^{-1}, and their % explained variances and mean accuracy for each frequency range

1300–1900 cm^{-1}			1000–3400 cm^{-1}		
Linear discriminant	% Explained variance	Mean accuracy	Linear discriminant	% Explained variance	Mean accuracy
LD1	94.8%	99.7% (10 splits, 3 repeats)	LD1	94.3%	82.3% (10 splits, 3 repeats)
LD2	4.5%		LD2	1.5%	

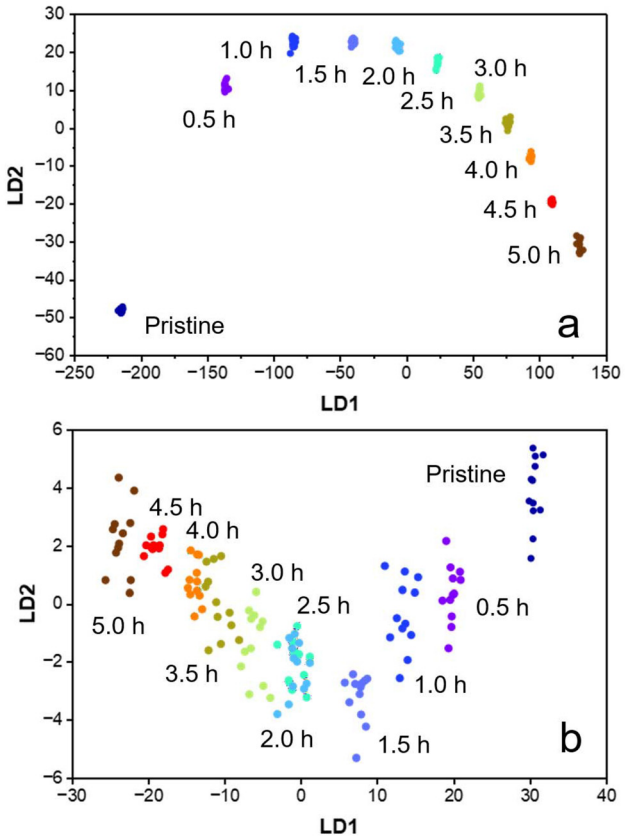

Fig. 5 LDA plots of the first two linear discriminants for the training set of normalized ATR-FTIR spectra from PTB7 films spin cast onto ZnSe IREs (512 scans, 4 cm^{-1} resolution, sample size n = 4, each collected in triplicate) with cumulative 30 min exposures to radiation from a solar simulator in the frequency regions of (a) 1300–1900, and (b) 1000–3400 cm^{-1}. Samples are color coded by accumulated solar simulator exposure time.

ting of the data and reduced prediction accuracy.[42,43] This problem of small sample size argues for the use of PCA prior to LDA to generate a reduced number of principal components as variables for the LDA training set such that the number of variables is less than the number of samples.[44]

To determine how many principal components to use for PCA-LDA, an approach based on stratified k-fold cross validation was used to evaluate accuracy for 10, 20, 30 and 40 principal components from PCA of the PTB7 spectral data in the 1300–1900 cm^{-1} region (Fig. 6). The metric used to determine the optimal test case was the mean accuracy scores calculated from repeated stratified k-fold cross validation of the linear discriminants with 10 splits and 3 repeats. The results show that as the number of principal components increases from 10 to 40, the mean accuracy improves from 91.1% to 100%. Seeking >99% mean accuracy, 40 principal components were used in subsequent PCA-LDA iterations, albeit admittedly at the risk of slight overfitting. Based on the data in Fig. 6, little accuracy would be lost by using 20 or 30 principal components with mean accuracies of 98.9% and 99.8% accuracy. The first two linear discriminants calculated from 40 principal components over each frequency range are shown in Fig. 7.

When trained with spectral data encompassing the 1000–3400 cm^{-1} region with 40 principal components is used for subsequent LDA, an equally satisfactory mean accuracy of 99.7% was calculated (Table 2). These mean accuracy scores are supported by box plot representations of the first two calculated LDs for each spectral region shown as Fig. S5 and S6 in the SI. For both spectral regions, the LD1 values of each degradation group have low spread and median values that do not overlap with each other, indicating a clear difference between groups. The LD2 values show some overlap of median values, especially for samples with short duration light exposure, but in general also have low spreads and distinct median values. These qualitative observations are confirmed by Analysis of Variance (ANOVA) testing shown by the results in Tables S2 and S4. At the $p < 0.05$ level, the population scores of the LDs in one or more of the degradation groups are significantly different from each other over both frequency regions. *Post hoc* Tukey's Honestly Significant Difference (HSD) testing (Tables S3 and S5) for means comparison for each group of LD scores reveals that all LD1 groups have significantly different means. The Tukey results for LD2 were nearly as satisfactory, with only three groups in each frequency region with mean values insignificant from another group. The statistical analysis of each calculated LD suggests that high mean accuracies should be expected for this model.

To further test the utility of ATR-FTIR as a predictive tool for assessment of PTB7 degradation, spectral datasets were obtained from two independent researchers as external test cases for the PCA-LDA model. The use of independent researchers for the collection and/or processing of the spectral test sets was implemented to simulate an end user of a future diagnostic tool. Each dataset consisted of PTB7 films subjected to a series of ten 30 min solar simulator exposures. Spectra were collected and processed in an identical manner to the training set with a total test sample size of n = 132.

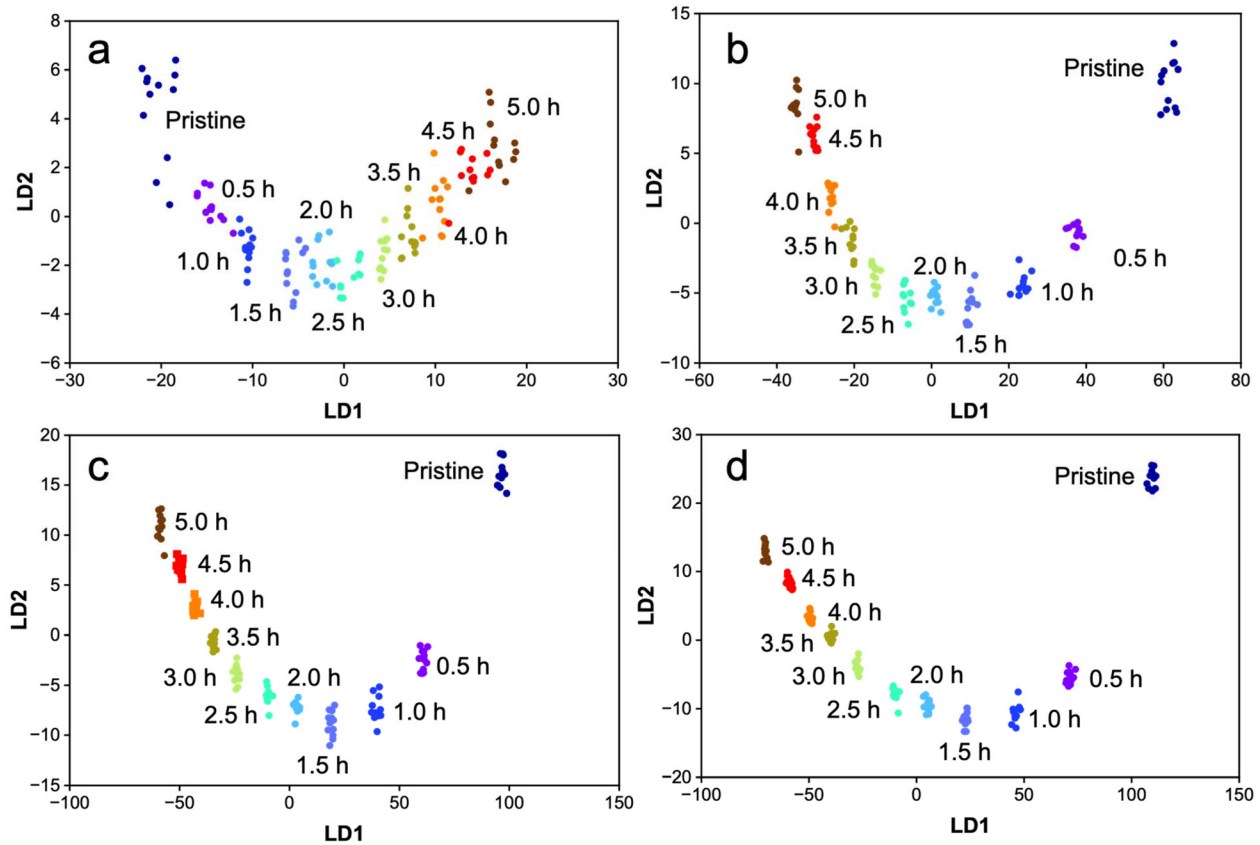

Fig. 6 LDA plots of the first two linear discriminants for the training set of normalized ATR-FTIR spectra from PTB7 films spin cast onto ZnSe IREs (512 scans, 4 cm^{-1} resolution, sample size n = 4, each collected in triplicate) with cumulative 30 min exposures to radiation from a solar simulator for the frequency region of 1300–1900 cm^{-1} using (a) 10, (b) 20, (c) 30, or (d) 40 principal components. Samples are color coded by accumulated solar simulator exposure time.

Test dataset 1 (TD1) was collected and spectral processing was performed by an independent researcher (Researcher 1) who was not involved in either experimental design or collection of the training set but who was familiar with characteristic spectral changes upon PTB7 photodegradation. After processing, spectra were deidentified before performing PCA-LDA. This test dataset contains contributions from both experimental and data processing variance. Test dataset 2 (TD2) was collected by the primary author of this work but processed by an independent researcher (Researcher 2). Researcher 2 had no prior experience with PTB7 photodegradation and was given deidentified raw spectral data to process. TD2 contains contributions from data processing variance only. This difference in skill level of the two researchers was done intentionally to generate testing data that would mimic the work of an average user. As with the data provided in TD1, the results in TD2 were de-identified again after processing but prior to performing PCA-LDA. Spectral data from each dataset are presented in Fig. 8.

For the spectral range of 1300–1900 cm^{-1}, the PCA-LDA model correctly predicts the specific 30 min exposure period classification of test dataset spectra 67.4% of the time. This accuracy is worse than the mean accuracy obtained from the k-fold cross validation (100.0%). However, further analysis reveals that the accuracy improves to 93.2% for boundaries of ±30 min (*i.e.* across three 30 min exposure periods) in radiant exposure. The accuracy of the model increases to 99.2% and 100% by expanding the acceptable exposure time boundaries to ±60 (*i.e.* across 5 exposure periods) and ±90 (*i.e.* across 7 exposure periods) min, respectively. Thus, these results demonstrate that the model can predict with acceptable accuracy degradation extent of an unknown sample to within ±30 min out of 5 h of total exposure. Recognizing that the protocol employed here represents accelerated degradation relative to what would occur in an actual device, this level of predictive accuracy is considered satisfactory.

As expected, when the frequency region subjected to PCA-LDA of the test data is increased to 1000–3400 cm^{-1}, the accuracy of the PCA-LDA model worsens. It only manages to correctly predict 62.1% of the samples, although allowing boundaries of ±30 min, ±60 min, and ±90 min results in respectable accuracy scores of 84.8%, 91.7%, and 95.5%, respectively. This decrease in performance aligns with the expectation that addition of low spectral information regions (*i.e.* no spectral activity) decreases model accuracy.

The most useful application of a classification tool for OPVs might arguably be a simple binary classification: degraded or

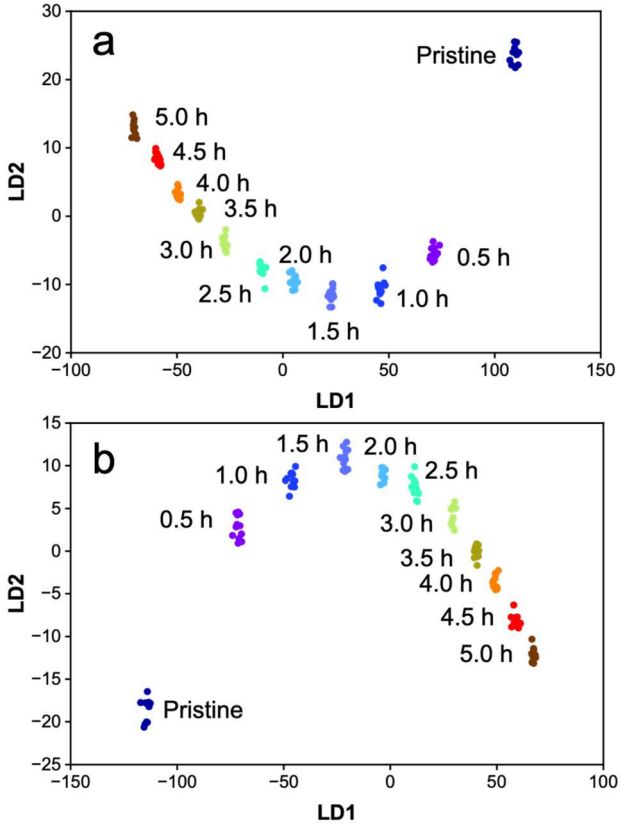

Fig. 7 PCA-LDA plots of the first two linear discriminants for the training set of normalized ATR-FTIR spectra from PTB7 films spin cast onto ZnSe IREs (512 scans, 4 cm^{-1} resolution, sample size n = 4, each collected in triplicate) with cumulative 30 min exposures to radiation from a solar simulator calculated from 40 principal components for the frequency range of (a) 1300–1900, and (b) 1000–3400 cm^{-1}. Samples are color coded by accumulated solar simulator exposure time.

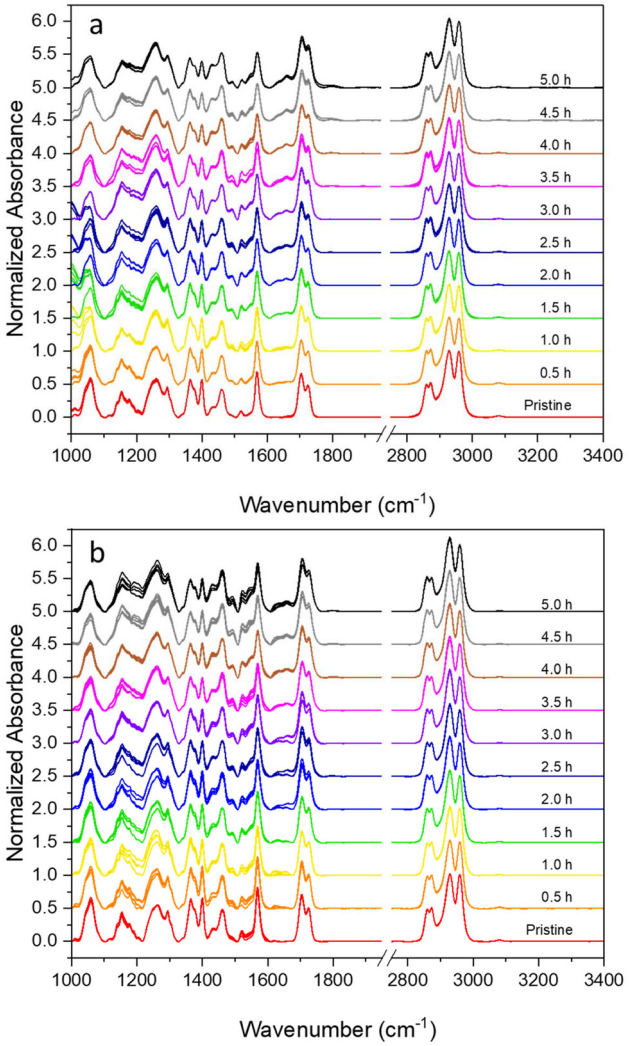

Fig. 8 Normalized ATR-FTIR spectra from PTB7 films spin cast onto ZnSe IREs (512 scans, 4 cm^{-1} resolution, sample size n = 2, each collected in triplicate) with cumulative 30 min exposures to radiation from a solar simulator. (a) Test dataset 1 (TD1), and (b) test dataset 2 (TD2).

not degraded. When analyzing the results from PCA-LDA of the 1300–1900 cm^{-1} region, the model correctly discriminates between pristine and degraded samples 100% of the time, *i.e.* all spectra from pristine films are accurately classified as pristine samples and no spectra from degraded films are classified as pristine samples. Increasing the frequency range of the spectral data used to 1000–3400 cm^{-1} still results in an impressive 89.4% accuracy for discrimination between pristine and degraded samples. This decrease in accuracy is due to the inclusion of low-information spectral regions, and the expanded frequency region, providing more opportunities for human inconsistencies during data processing to affect calculated LD scores of the unknown samples, and thus, affect the predictive outcome. A summary of the classification results is given in Table 3. Accuracy scores for the original groupings along with the evaluation of binary distinction were also calculated individually for each dataset and are reported in Tables S6–S9 of the SI.

Table 2 Calculated linear discriminants using 40 principal components from PCA of PTB7 ATR-FTIR spectral data between 1300–1900 and 1000–3400 cm^{-1}, and their % explained variances and mean accuracy for each frequency range

1300–1900 cm^{-1}			1000–3400 cm^{-1}		
Linear discriminant	% Explained variance	Mean accuracy	Linear discriminant	% Explained variance	Mean accuracy
LD1	95.8%	100.0% (10 splits, 3 repeats)	LD1	96.8%	99.7% (10 splits, 3 repeats)
LD2	3.6%		LD2	2.6%	

Table 3 Accuracy scores for the PCA-LDA model applied to PTB7 spectral data for photodegradation with data groupings by 30 min radiant exposure intervals or by binary not degraded/degraded groups

Grouping	1300–1900 cm^{-1}	1000–3400 cm^{-2}
30 min exposure groups	67.4%	62.1%
±30 min	93.2%	84.8%
±60 min	99.2%	91.7%
±90 min	100%	95.5%
Binary degraded/not degraded groups	100%	89.4%

These results suggest that PCA-LDA can be used successfully to classify unknown photodegraded OSC films based on their total radiant exposure time. The accuracy scores from the 1300–1900 cm^{-1} range are particularly promising and suggest that a future multivariate analysis-based diagnostic tool for OSC photodegradation is feasible. We note that degradation of the PTB7 films was induced using an accelerated degradation protocol by exposure of the entire film to ambient atmospheric conditions while under illumination. Obviously, active layer films in real devices will undergo degradation much more slowly. In this context, the choice here of 30 min radiant exposure intervals was somewhat arbitrary and made mainly for experimental convenience. Given the subtle nature of the spectral changes observed during degradation, it is not reasonable to expect extremely high accuracy in precisely predicting specific 30 min exposure interval groups by the PCA-LDA model used. Although exposure intervals longer than those tested here may result in better precise classification accuracy, this cannot be definitively proven without further experimentation under these different conditions. Nonetheless, reasonable accuracy is obtained, which, when expanded to the time scales of a real OSC device, strongly supports the potential of a viable diagnostic tool based on this approach.

Conclusions

This work represents a proof-of-concept demonstration that a PCA-LDA model can accurately predict whether an unknown film of PTB7 has undergone photodegradation, and if so, to what extent, by subjecting it to an accelerated degradation protocol through radiant exposure in air to a solar simulator. Using the spectral data in the frequency range of 1300–1900 cm^{-1}, the accuracy of correctly classifying unknown samples to the correct 30 min exposure interval is 67.4%. However, the accuracy improves to >90% when samples were classified to within ±30 min out of a total exposure of 5 h. Using the spectral data over the wider frequency range of 1000–3400 cm^{-1}, which includes a several hundred cm^{-1} low information content spectrally-silent region, the PCA-LDA model correctly classifies only 62.1% of samples to the specific 30 min exposure group. However, >90% of samples were correctly classified to within ±60 min out of the total exposure of 5 h. For simple binary classification between pristine and degraded samples, the model classifies unknown spectral data with high accuracy, achieving 100% accuracy when applied to spectral data in the frequency range of 1300–1900 cm^{-1} and 89.4% accuracy when applied to data in the frequency range of 1000–3400 cm^{-1}. Overall, the success of these experiments provides a strong foundation for the future of data-driven predictive analysis for the OSC field.

Efforts to design an experimental architectural that allows ATR-FTIR spectral sampling during application of perturbations by applied voltage and/or exposure to light in an *operando* platform are being pursued actively in this laboratory and will be reported at a later date. That said, field deployment of any vibrational spectroscopic probe of degradation will likely require additional advances that allow reflectance-based approaches to be used through the optically transparent side of a fully encapsulated device. The work reported here, and recent[23,45] and ongoing efforts in this laboratory, justify optimism that such approaches will eventually be successful given the demonstrated ability of vibrational spectroscopy coupled with multivariate analysis tools to reliably differentiate very small differences between complex spectra of OSC-based systems.

Author contributions

JEP and SMT conceptualized the work. SMT, TJB and KTS performed the experiments. SMT performed the majority of the spectral data analysis. SMT and JEP wrote and edited the manuscript. All authors approved the final version of the manuscript.

Conflicts of interest

There are no conflicts to declare.

Data availability

ATR-FTIR spectral data for this article are available on Github at https://github.com/styler808/OSC-Chemometrics along with the specialized Python code for the PCA-LDA analysis.

Supplementary information (SI) containing additional PTB7 ATR-FTIR data along with vibrational assignments, a brief primer on 2D-COS, additional statistical analysis of chemometric results, and individual test dataset acuracy results is available. See DOI: https://doi.org/10.1039/d5an01007a.

Acknowledgements

The authors acknowledge support of this research by the U.S. National Science Foundation under award DMR-2003631. SMT acknowledges financial support through an ARCS Foundation Scholarship. AFM data were acquired in the University of Arizona Chemistry & Biochemistry W. M. Keck Center for Nano-Scale Imaging, RRID:SCR_022884.

References

1 S. Holliday, Y. Li and C. K. Luscombe, *Prog. Polym. Sci.*, 2017, **70**, 34–51.
2 Y. Li, X. Guo, Z. Peng, B. Qu, H. Yan, H. Ade, M. Zhang and S. R. Forrest, *Proc. Natl. Acad. Sci. U. S. A.*, 2020, **117**, 21147–21154.
3 R. Meitzner, U. S. Schubert and H. Hoppe, *Adv. Energy Mater.*, 2020, **11**, 2002551.
4 X. Xu, L. Yu, H. Meng, L. Dai, H. Yan, R. Li and Q. Peng, *Adv. Funct. Mater.*, 2021, **32**, 2108797.
5 L. Zhan, S. Li, X. Xia, Y. Li, X. Lu, L. Zuo, M. Shi and H. Chen, *Adv. Mater.*, 2021, **33**, e2007231.
6 Q. Liu, Y. Jiang, K. Jin, J. Qin, J. Xu, W. Li, J. Xiong, J. Liu, Z. Xiao, K. Sun, S. Yang, X. Zhang and L. Ding, *Sci. Bull.*, 2020, **65**, 272–275.
7 M. Zhang, L. Zhu, G. Zhou, T. Hao, C. Qiu, Z. Zhao, Q. Hu, B. W. Larson, H. Zhu, Z. Ma, Z. Tang, W. Feng, Y. Zhang, T. P. Russell and F. Liu, *Nat. Commun.*, 2021, **12**, 309.
8 A. Armin, W. Li, O. J. Sandberg, Z. Xiao, L. Ding, J. Nelson, D. Neher, K. Vandewal, S. Shoaee, T. Wang, H. Ade, T. Heumüller, C. Brabec and P. Meredith, *Adv. Energy Mater.*, 2021, **11**, 2003570.
9 S. Guo, Y. Hu, M. Qin, J. Li, Y. Wang, J. Qin and P. Cheng, *Mater. Horiz.*, 2022, **9**, 2097–2108.
10 M. Jørgensen, K. Norrman and F. C. Krebs, *Sol. Energy Mater. Sol. Cells*, 2008, **92**, 686–714.
11 Y. Li, T. Li and Y. Lin, *Mater. Chem. Front.*, 2021, **5**, 2907–2930.
12 M. Aghaei, A. Fairbrother, A. Gok, S. Ahmad, S. Kazim, K. Lobato, G. Oreski, A. Reinders, J. Schmitz, M. Theelen, P. Yilmaz and J. Kettle, *Renewable Sustainable Energy Rev.*, 2022, **159**, 112160.
13 Y. Zhou, C. Fuentes-Hernandez, T. M. Khan, J. C. Liu, J. Hsu, J. W. Shim, A. Dindar, J. P. Youngblood, R. J. Moon and B. Kippelen, *Sci. Rep.*, 2013, **3**, 1536.
14 J. A. Tsanakas, A. Heide, T. Radavičius, J. Denafas, E. Lemaire, K. Wang, J. Poortmans and E. Voroshazi, *Prog. Photovoltaics*, 2019, **28**, 454–464.
15 D. Pelliccia, Classification of NIR Spectra by Linear Discriminant Analysis in Python, https://nirpyresearch.com/classification-nir-spectra-linear-discriminant-analysis-python/.
16 S. M. Tyler, OSC-Chemometrics, https://github.com/styler808/OSC-Chemometrics, (accessed 09/17/2025).
17 J. Razzell-Hollis, J. Wade, W. C. Tsoi, Y. Soon, J. Durrant and J.-S. Kim, *J. Mater. Chem. A*, 2014, **2**, 20189–20195.
18 S. Shah, R. Biswas, T. Koschny and V. Dalal, *Nanoscale*, 2017, **9**, 8665–8673.
19 S. Kim, M. A. M. Rashid, T. Ko, K. Ahn, Y. Shin, S. Nah, M. H. Kim, B. Kim, K. Kwak and M. Cho, *J. Phys. Chem. C*, 2020, **124**, 2762–2770.
20 D. M. Schwaiger, W. Lohstroh, M. Wolf, C. J. Garvey and P. Müller-Buschbaum, *J. Polym. Sci.*, 2023, **61**, 1660–1674.
21 S. Holliday and C. K. Luscombe, *Adv. Electron. Mater.*, 2018, **4**, 1700416.
22 B. J. Tremolet de Villers, K. A. O'Hara, D. P. Ostrowski, P. H. Biddle, S. E. Shaheen, M. L. Chabinyc, D. C. Olson and N. Kopidakis, *Chem. Mater.*, 2016, **28**, 876–884.
23 T. J. Blackburn, S. M. Tyler and J. E. Pemberton, *J. Phys. Chem. C*, 2025, **129**, 19320–19335.
24 S. Park, S. H. Kim, H. H. Choi, B. Kang and K. Cho, *Adv. Funct. Mater.*, 2020, **30**, 1904590.
25 X. Song, M. G. Fanelli, J. M. Cook, F. Bai and C. A. Parish, *J. Phys. Chem. A*, 2012, **116**, 4934–4946.
26 I. Aped, Y. Mazuz and C. N. Sukenik, *Beilstein J. Nanotechnol.*, 2012, **3**, 213–220.
27 Y. W. Soon, H. Cho, J. Low, H. Bronstein, I. McCulloch and J. R. Durrant, *Chem. Commun.*, 2013, **49**, 1291–1293.
28 I. Noda, A. E. Dowrey, C. Marcott, G. M. Story and Y. Ozaki, *Appl. Spectrosc.*, 2000, **54**, 236A–248A.
29 P. D. B. Harrington, A. Urbas and P. J. Tandler, *Chemom. Intell. Lab. Syst.*, 2000, **50**, 149–174.
30 M. A. Czarnecki, *Appl. Spectrosc.*, 2003, **57**, 991–995.
31 Y. Ozaki, S. Šašic, T. Tanaka and I. Noda, *Bull. Chem. Soc. Jpn.*, 2001, **74**, 1–17.
32 I. Noda, *Appl. Spectrosc.*, 1993, **47**, 1329–1336.
33 I. Noda, in *Frontiers and Advances in Molecular Spectroscopy*, ed. J. Laane, Elsevier, Amsterdam, Netherlands, 2018, pp. 47–75, DOI: 10.1016/B978-0-12-811220-5.00002-2.
34 M. A. Czarnecki, *Appl. Spectrosc.*, 2020, **74**, 894–899.
35 J. Semmler, P. W. Yang and G. E. Crawford, *Vib. Spectrosc.*, 1991, **2**, 189–203.
36 V. Gomez-Serrano, J. Pastor-Villegas, A. Perez-Florindo, C. Duran-Valle and C. Valenzuela-Calahorro, *J. Anal. Appl. Pyrolysis*, 1996, **36**, 71–80.
37 L. I. Smith, *A tutorial on Principal Components Analysis*, University of Otago, Dunedin, New Zealand, 2002.
38 S. Raschka, Implementing a Principal Component Analysis (PCA) - in Python, step by step, https://sebastianraschka.com/Articles/2014_pca_step_by_step.html#mean_vec (accessed 12/10/2025).
39 S. Raschka, Linear Discriminant Analysis - Bit by Bit, https://sebastianraschka.com/Articles/2014_python_lda.html (accessed 12/10/2025).
40 K. Yasar, Principal Component Analysis, https://medium.com/@kyasar.mail/pca-principal-component-analysis-729068e28ec8, (accessed 12/10/2025).
41 C. L. M. Morais, K. M. G. Lima, M. Singh and F. L. Martin, *Nat. Protoc.*, 2020, **15**, 2143–2162.
42 K. Fukunaga, in *Introduction to Statistical Pattern Recognition*, Academic Press, San Diego, CA, 2nd edn, 1990, ch. Chapter 2, pp. 39–40, DOI: 10.1016/C2009-0-27872-X.
43 C. L. M. Morais, M. Paraskevaidi, L. Cui, N. J. Fullwood, M. Isabelle, K. M. G. Lima, P. L. Martin-Hirsch, H. Sreedhar, J. Trevisan, M. J. Walsh, D. Zhang, Y. G. Zhu and F. L. Martin, *Nat. Protoc.*, 2019, **14**, 1546–1577.
44 D. L. Swets and J. Weng, *IEEE Trans. Pattern Anal. Mach. Intell.*, 1996, **18**, 831–836.
45 S. M. Tyler and J. E. Pemberton, *J. Mater. Chem. C*, 2025, **13**, 16699–16711.